CONDENSED MATTER PHYSICS

Giant spin signals in chemically functionalized multiwall carbon nanotubes

Roméo Bonnet[1]*, Pascal Martin[2], Stéphan Suffit[1], Philippe Lafarge[1], Aurélien Lherbier[3†], Jean-Christophe Charlier[3], Maria Luisa Della Rocca[1], Clément Barraud[1†]

Transporting quantum information such as the spin information over micrometric or even millimetric distances is a strong requirement for the next-generation electronic circuits such as low-voltage spin-logic devices. This crucial step of transportation remains delicate in nontopologically protected systems because of the volatile nature of spin states. Here, a beneficial combination of different phenomena is used to approach this sought-after milestone for the beyond–Complementary Metal Oxide Semiconductor (CMOS) technology roadmap. First, a strongly spin-polarized charge current is injected using highly spin-polarized hybridized states emerging at the complex ferromagnetic metal/molecule interfaces. Second, the spin information is brought toward the conducting inner shells of a multiwall carbon nanotube used as a confined nanoguide benefiting from both weak spin-orbit and hyperfine interactions. The spin information is finally electrically converted because of a strong magnetoresistive effect. The experimental results are also supported by calculations qualitatively revealing exceptional spin transport properties of this system.

INTRODUCTION

Future spin circuits are foreseen to largely overcome performances of pure charge-based circuits mainly by drastically lowering the power consumption and because of their nonvolatility offered by magnetic materials (*1*–*4*). The core operation of those devices is to electrically propagate the spin information as a spin accumulation ($\mu_\uparrow - \mu_\downarrow \neq 0$, where μ represents the chemical potential for both spin direction) in an array of different nanomagnets or magnetic tunnel junctions. Those magnetic elements will then act on the spin accumulation profile. Operations and electrical measurements as voltages of the chemical potential profile over the entire array can form logic operations and logic states (*1*). Several competing viable alternatives exist to inject spins such as the spin pumping method (*5*), spin Seebeck-Nernst effects (*6*), spin Hall effects (*7*), polarized optical excitations (*8*), and excitations of magnons (*9*) or electrically from a spin source such as ferromagnetic (FM) elements (Co, Fe, or Ni, for instance) (*10*). Here, we focus only on the electrical spin injection method (*11*), which combines charge and spin transport. In such experiments, propagating a robust spin signal is challenging as two physical phenomena have to play in concert: a strong spin polarization of the injected/detected current and a long spin diffusion length generally associated to a weak spin scattering within the transport platform (*12*). In nontopological solids, spin-orbit coupling and hyperfine interactions with nuclear spins are responsible for the spin relaxation. Successful attempts to reach long spin transport distances (>10 μm) were made in the past few years by inserting carbon-based nanomaterials (*13*–*19*) as transport platforms. For instance, Hueso *et al.* (*20*) and Dlubak *et al.* (*21*) have reported substantial magnetoresistance (MR) $\Delta R = R_{AP} - R_P$ ($\approx 10^6$ ohms) in carbon nanotubes (CNTs) and SiC graphene–based spin valves, respectively. Those spin signals were associated to extraordinary long spin diffusion lengths above 70 μm. Those pioneer results have highlighted the potential of carbon-based π-conjugated nanomaterials as spin transport platforms (*12*), initiating a budding and intense field of research recently reviewed in (*22*). This success can be mainly attributed not only to the weak spin scattering but also to the high carrier's mobility present in π-conjugated C-based materials (*23*). Spin injection/detection processes at FM electrode/CNT and FM electrode/graphene interfaces have been widely scrutinized to attain efficient rates (*17*, *24*–*26*). Because of the earlier work concerning spin injection at FM metal/semiconductor interfaces (*27*) and the so-called impedance mismatch issue, those studies have also pointed out the necessity not only to accurately control the interface properties (*21*, *24*) but also to favor confined architectures for the devices (*28*). Those two key elements are described in the following. Transparent interfaces (i.e., without any injection barrier) between the spin transport material and the FM electrodes should be ideal for efficiently detecting spins. However, from the injection point of view, transparent interfaces are invasive and thus strongly affect the injected current because of backflowing into the electrodes, where charges suffer most from relaxation (*12*). Opaque interfaces (i.e., with an injection barrier) may enhance the dwell time and favor spin relaxation within the transport platform. Spin injection/detection from an FM metal into CNTs and graphene was finally found to be optimized with interfacial resistances of the order of 10^8 ohms (*12*, *21*). For the specific case of CNTs, the direct contact of the FM metal over the CNTs was mostly privileged, leading to contact resistances from few 10^3 to 10^7 ohms (*29*–*32*) but to rather limited spin diffusion lengths up to few micrometers. In this configuration, proximity effects with the FM electrodes may also induce a local spin splitting of the carbon nanomaterial band structure (*33*). In addition, the device's architecture also plays a key role. Confined geometries in a two-probe configuration are usually favored to prevent spin escape from the sides of the devices (*28*). Despite all the research efforts made in those directions, a fundamental question remains about the intrinsic values of spin transport lengths in graphene and CNTs. As those nanomaterials can almost be considered as "surfaces," the electronics and spintronics properties are very sensitive to the interaction with the substrate or to the electrodes or even to the nanofabrication process. Presently, no experiment is

[1]Université de Paris, Laboratoire Matériaux et Phénomènes Quantiques, CNRS, UMR 7162, 75013 Paris, France. [2]Université de Paris, ITODYS, CNRS, UMR 7086, 75013 Paris, France. [3]Institute of Condensed Matter and Nanosciences (IMCN), Université catholique de Louvain (UCLouvain), B-1348 Louvain-la-Neuve, Belgium. *Present address: Université de Paris, ITODYS, CNRS, UMR 7086, 75013 Paris, France. †Corresponding author. Email: aurelien.lherbier@uclouvain.be (A.L.); clement.barraud@u-paris.fr (C.B.)

able to determine the value of the intrinsic spin diffusion length in these carbon nanostructures. It is thus highly probable that the 100 to 200 μm reported up to now do not reach the upper theoretical limit (*21*). In the present work, properties of individual multiwall CNTs (MWCNTs) for which the outershell is covalently functionalized by molecules are explored as confined nanoguides for spin transport. As demonstrated further, the aim of this chemical functionalization is threefold: first, increasing the interfacial resistance between the FM metal and the MWCNT up to values ranging between 10^7 and 10^{10} ohms to reach an efficient regime for the spin injection (*34*); second, benefiting from the spin-dependent hybridized molecular states at the FM/molecule interface (*35*) to attain very strong interfacial spin polarizations close to ±100% and thus intense magnetoresistive signals (*36*); third, pushing the injected charges toward the protected inner shells of the MWCNT to increase the spin lifetime.

RESULTS AND DISCUSSION

Electronic impact of the chemical functionalization of the outershell of the MWCNT

In this work, nitrobenzene (NB) diazonium (NBD) molecules, one of the simplest diazonium compound, are used to functionalize the surface of large-diameter (>60 nm) MWCNTs. The experimental details of the chemical functionalization are fully described and presented in Materials and Methods and also in (*34*). Upon functionalization, the NBD molecule loses its N_2 tail to form a highly reactive NB radical, as depicted in fig. S1C. As revealed by a representative high-resolution transmission electron microscopy image presented in Fig. 1A, the NB radicals are only reacting with the outershell of the MWCNT in the experimental conditions. This peculiar reactivity was also previously demonstrated for double-wall CNTs (DWCNTs) (*37*). To get a better overall view, the expected functionalization is also schematized in Fig. 1B for the case of a small-diameter DWCNT for clarity reason. The estimated grafting surface density is in the range of 10^{-10} to 10^{-9} mol cm^{-2} (*38*). The systems illustrated in Fig. 1D are therefore representative of the experimental molecular surface density. To understand the impact of the chemical functionalization on the electronic properties of MWCNTs, we performed first-principles calculations using ab initio density functional theory (DFT; see Materials and Methods for technical details). Although H-saturated NB does not exhibit any magnetic moment (see fig. S1B), its radical develops a magnetic moment of 1 bohr magneton (μ_B) with ~93% located on the dangling bond (see fig. S1C). This radical moiety can be stabilized by the formation of dimers in the solution, or it can react and can be grafted onto the outershell of the large-diameter MWCNT, the latter being modeled by a graphene monolayer in the DFT calculations as shown in Fig. 1 (C and D). At the end of this functionalization process, the NB molecule is stabilized over the MWCNT outershell forming a saturated chemical bond with a C atom from the outershell.

As a physical consequence, upon functionalization, each affected C atom of the outershell of the MWCNT modifies its electronic configuration from a conducting sp^2 to an insulating sp^3 hybridization, which should render the outershell of the MWCNT quite insulating. Pristine graphene is nonmagnetic (as calculated in fig. S1D), but upon functionalization by one NB molecule on a given sublattice, the system could acquire a net magnetic moment (see Fig. 1C) (*39*). In contrast to physisorption where the magnetic moment stays fully localized on the π-π stacked molecule (see fig. S1F), in the case of NB chemisorption, the magnetic moment is well transferred into graphene, though slightly reduced to 0.96 μ_B (see Fig. 1C). As illustrated in Fig. 1C, two spin-split almost-flat bands are located close to the Fermi level in a range of ~200 meV with ideal spin polarization P passing from −100% to +100%. However, as this magnetization propagates into graphene from a given NB molecule, it is important to check how it will interact with the nearest-neighbor molecule. As demonstrated in literature, for instance, in case of hydrogen (*40*, *41*), the choice of the sublattice as anchoring site and the distance between two grafted molecules is a key parameter for determining these interactions. As expected, when restoring the balance between the two sublattices, the magnetic moment vanishes as observed in Fig. 1D for the case of two NB molecules on sublattice "A" and two others on sublattice "B" (see also fig. S2). Experimentally, as the density of anchoring A and B sites for NB molecules in the outershell of the MWCNT is identical and that NB radicals react randomly with both sites during the functionalization process (*34*, *37*, *42*), a globally vanishing total magnetic moment is expected. Residual but very localized paramagnetic states cannot be fully excluded, but no proof of their existence is directly measured in this study. Also, the influence of those residual magnetic moments on the spin transport is not described here in this article. As discussed below, the spin signal transport is believed to occur mostly in the next inner shells free of functionalization for which the impact of those hypothetical paramagnetic states should thus be anyway limited. Last, this optimized functionalization process has also been experimentally demonstrated in a previous study (*34*) to increase the injection resistance above the 10^6 ohm range within the ideal window for an efficient spin injection in MWCNTs (*20*) and SiC graphene (*12*).

Spin transport measurements at cryogenic temperatures

The experimental details related to both the nanofabrication procedures and the magnetotransport measurements can be found in Materials and Methods. Two samples named A and B are presented in the following. Sample A is fabricated with Ni contacts, and sample B is fabricated with Co contacts. Those two FM metals were chosen to probe different interfacial spin polarization and coupling with the molecules as widely studied before (*36*, *43*). The selective switching of their magnetizations is obtained by tuning the shape anisotropy with different electrode widths (500 and 200 nm). Because the length of the large-diameter MWCNTs is quite limited (few micrometers), the electrode separation is 900 nm for sample A and 800 nm for sample B.

Figure 2A depicts a schematic of the magnetoresistive devices studied here supported by a scanning electron microscopy image of sample B shown in Fig. 2B. The local MR signal defined as $MR = \frac{R_{AP} - R_P}{R_P} = \frac{I_P - I_{AP}}{I_{AP}}$ measured at cryogenic temperatures and at −140 mV in sample A between two nickel (Ni) electrodes is plotted in Fig. 2C. R_{AP} is the electrical resistance measured in the antiparallel configuration of the magnetizations, and R_P is the resistance measured at $H = 0$ T in the parallel configuration of the magnetizations. The low-temperature resistance reaches 10^9 to 10^{10} ohms for this first sample. It is only due to the presence of the molecular injection barrier as demonstrated in (*34*). The blue (black) dots are measured while sweeping the magnetic field toward positive (negative) values. This measurement exhibits important variations of the device's MR including negative values going at maximum down to −40%. This negative sign of the MR might be unexpected as both interfaces are

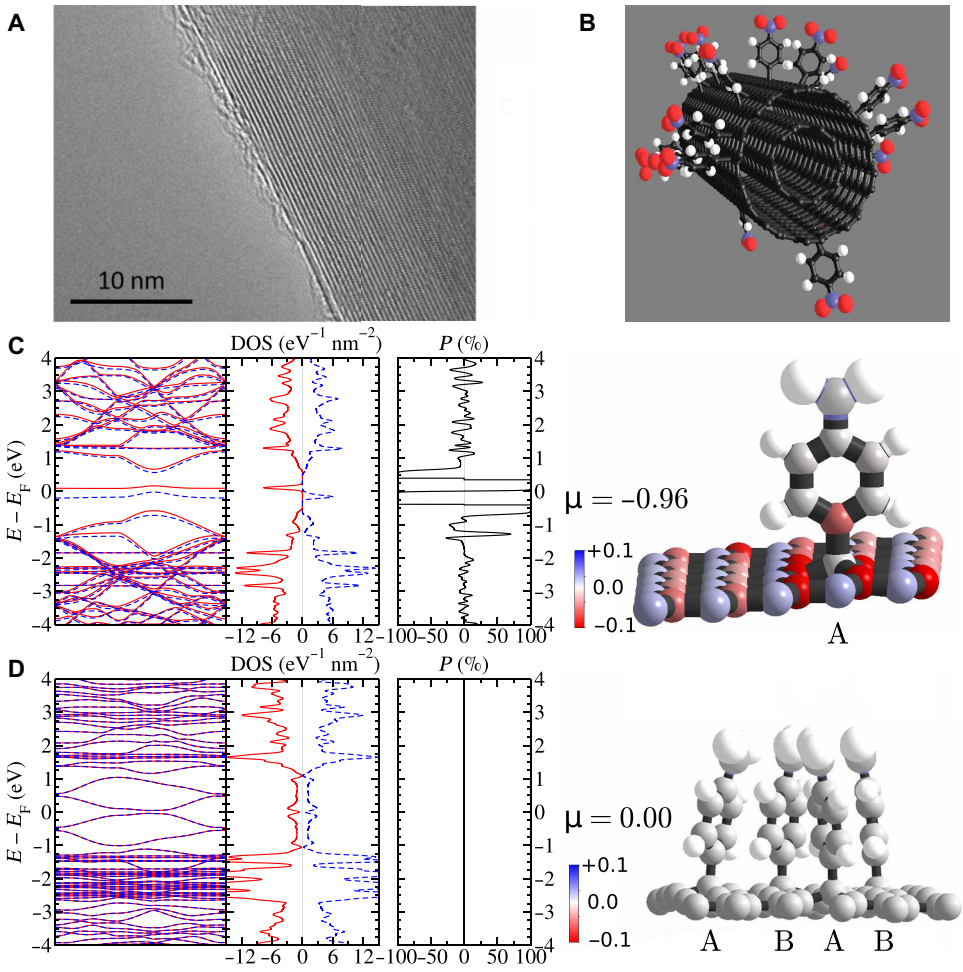

Fig. 1. Chemically functionalized MWCNT as a nanoguide for spin transport. (**A**) High-resolution transmission electron microscopy image of an individual MWCNT functionalized by NB molecules. (**B**) Three-dimensional (3D) schematics of (5,5)@(10,10) DWCNT functionalized by 19 NB molecules. (**C** and **D**) Spin-resolved electronic band structures, density of states (DOS), and associated spin polarization of (C) one NB molecule chemisorbed onto A sublattice of graphene and (D) four NB molecules chemisorbed onto both A and B sublattices of graphene. Down (majority) and up (minority) spins are represented by dashed blue and solid red lines, respectively. The total magnetic moment per cell is indicated by μ (in units of bohr magnetron μ_B), and the magnetic moment per atom is represented with a color code on the right panel (see color map with range restricted to [−0.1;+0.1] μ_B).

supposed to be the same, but it will be explained in the next part. It also reveals some interesting magnetoresistive features that can be identified and classified into three categories. First, a progressive decrease of the resistance at high magnetic fields (> 50 mT) is reported. This high-field MR has already been observed in MWCNTs in the case of applied transverse magnetic fields and was attributed to weak localization effects (*44*). In fig. S3, a high-field MR plot up to 1 T is also shown, in perfect agreement with those reported in (*44*). Second, the two regions with very large and sharp variations of resistances around ±40 mT display similar amplitudes and, respectively, appear at positive (negative) magnetic field when the magnetic field is swept toward positive (negative) values. This behavior is typically the signature of spin transport in a spin-valve configuration (*20*). It allows us to identify the coercive fields corresponding to both electrodes. The largest coercive field is attributed to the narrowest magnetic electrode. The lowest state of resistance located in between −40 and −50 mT corresponds to the antiparallel configurations of the magnetizations (represented by yellow arrows in Fig. 2C). Last, weak positive MR (<5%) can be observed at low magnetic field ($|H| < 30$ mT). In opposition to the spin-valve effect, this magnetoresistive effect persists and could even reverse its sign when the magnetic field is rotated away from the electrodes' magnetization easy axis (see the angular dependence presented in fig. S5). The results presented in fig. S5 strongly indicate a tunneling anisotropic MR (TAMR) effect associated to the FM electrode/molecule interfaces (*45*, *46*). TAMR effects of similar intensity have previously been reported also at polycrystalline FM metal/molecule interfaces (*45*, *47*, *48*). Strongly supported by the angular dependence, all those arguments combined together demonstrate that the magnetoresistive effect of −40% can be unambiguously attributed to spin transport through the device. Those spin-dependent transport effects have also been reproduced in a second sample named sample B with cobalt (Co) electrodes, revealing the robust nature of the MR (see fig. S6). The local MR measurements reported in fig. S6C also present important MR effects down to −20%. The low-temperature resistance reaches 10^7 ohms for this second sample. However, the coercive

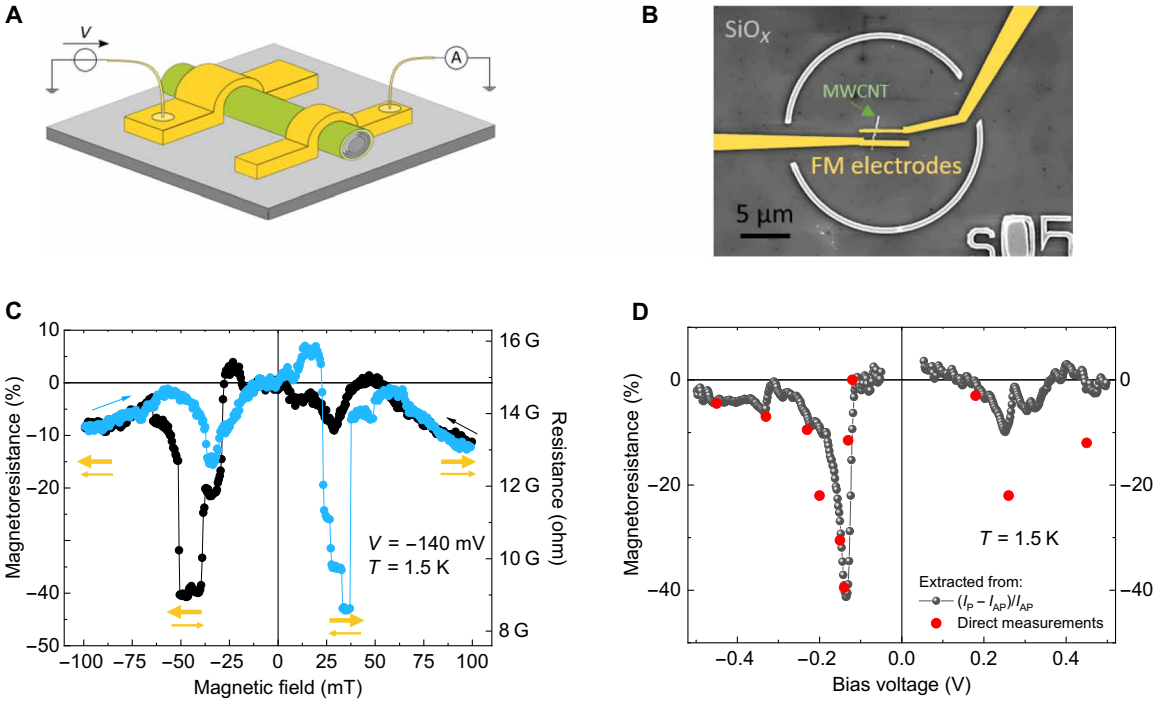

Fig. 2. Large negative MR signal. (**A**) 3D schematics of the two-probe spin transport device. (**B**) Colored scanning electron microscopy image of device B (with Co electrodes in yellow). (**C**) MR signal of −40% measured at −140 mV and $T = 1.5$ K in sample A. Arrows in yellow indicate the relative orientation of the electrodes' magnetizations. The thinnest one represents the narrowest FM electrode. (**D**) Bias dependence of the MR signal at $T = 1.5$ K for sample A. Dark gray dots are extracted from the MR formula $MR = \frac{I_P - I_{AP}}{I_{AP}}$ applied to the *I-V* characteristics measured in the parallel (I_P at $H = 0$ T) and antiparallel (I_{AP} at $H = -40$ mT) configurations (see fig. S4). Red dots represent the direct measurements of the MR's amplitude for various bias voltages from the MR characteristics such as plotted in Fig. 3C and fig. S7.

fields are less defined, in particular for the sweep toward the negative values of the magnetic field. It is possible to identify in fig. S6C two regions corresponding to an antiparallel configuration of the magnetizations, which again indicate spin transport between the two magnetic electrodes.

The identification of the parallel and antiparallel configurations of the magnetization allows the proper use of the MR formula $MR = \frac{I_P - I_{AP}}{I_{AP}}$ (*49*) to determine the dependence of the MR as a function of the applied bias voltage. The two *I-V* and *G-V* characteristics measured in the parallel and antiparallel states of the magnetizations are shown in figs. S4 and S6A for samples A and B, respectively. The bias voltage dependence is reported in Fig. 2D and fig. S6B for samples A and B, respectively. Different MR characteristics for sample A are also shown in fig. S7 (A to C) for $V = -120$ mV (0%), −200 mV (−20%), and −130 mV (−12%), respectively. The extracted bias dependence of the MR (dark gray dots) is found to be in excellent agreement with the values of MR extracted from the direct measurements of MR characteristics (red dots in Fig. 2D). In both samples, a strong dependence of the MR is observed with respect to the applied bias voltage. In opposition to what is typically presented in the literature for MWCNTs or even standard magnetic tunnel junctions (*20*, *50*), the maximum values of the MR do not appear close to zero bias but rather around specific values of energy [−140 mV for sample A (Ni contacts) and +130 mV for sample B (Co contacts)]. A change of sign of the MR is even measured in sample B. No evidence of gate voltage dependence is reported, as illustrated in fig. S8, for a bare large-diameter MWCNT excluding coulomb blockade effects, as expected due to the metallic nature of these multiwall tubes.

Spin-polarized calculations of interfaces and MR calculations

To better understand the spin injection at the magnetic electrode/functionalized MWCNT interface, we incorporate a Ni (100) slab composed of three atomic layers in the simulation cell above the NB molecules grafted on graphene. Similarly to the situation in Fig. 1D where sublattices were balanced resulting in no magnetic moment in the graphene layer, the case of two NB molecules grafted on each graphene sublattices is considered here (see Fig. 3B). Both the magnetic moment and spin polarization per atomic layer are computed as presented in Fig. 3 (A and B). It is important to note that those results should be considered from a qualitative point of view as they may fluctuate according to computational methods and atomic details of the interface. For instance, in Fig. 3B, the magnetic moment per Ni atom is ~0.88 μ_B in the outer layer and ~0.69 μ_B in the inner layer of the slab. This should be compared to the value of 0.75 μ_B per atom in bulk (see fig. S1A). The specific choice of an ideal Ni (100) surface will eventually not have a strong influence on the simulation of the MR as the key parameter to induce rapid variations around Fermi level of the spin polarization, including sign change, is brought by the spin-dependent local hybridization of the NB molecular orbitals (*51*). The hybridization of the molecules with the Ni surface induces a spin-dependent shift and broadening of its molecular orbitals (*36*, *52*). Note that in contrast to Fig. 1D, the oxygen atoms of the NB molecules acquire local positive magnetic moment due to the hybridization effects with the Ni surface. As shown in Fig. 3A, the calculated band structures and density of states projected onto each atomic layers allow us to access the energy-resolved spin polarization per atomic layers, labeled from [1] to [6], of the

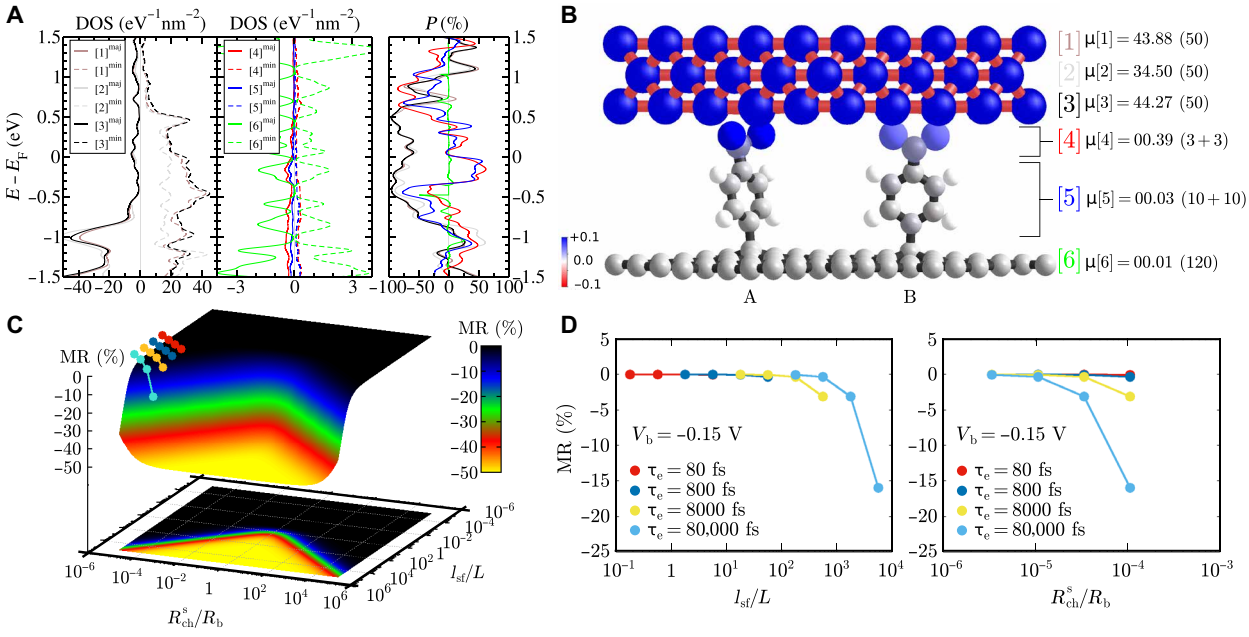

Fig. 3. Simulation of the spin transport properties. (**A** and **B**) Ni/NB/graphene interface. (A) Spin-resolved band structures, DOS, and associated spin polarization per atomic layers [indexed from [1] to [6]; see (B)] of the interface between a (100) Ni surface slab composed of three atomic layers and two NB molecules chemisorbed onto A and B sublattices of graphene. Up (majority) and down (minority) spins are represented by solid and dashed lines. The magnetic moment per atomic layer is indicated in (B) by μ together with the number of atoms per layer in parenthesis. The atomic-resolved magnetic moment is represented by a color code on the atoms (see color map with range restricted to [−0.1;+0.1] μ_B). (**C**) 3D plot of $MR^{\text{ideal spin polarizations}}$ as derived from the model in Eq. 3, i.e., for maximal spin polarization ($\gamma_L = 1$; $\gamma_R = -1$), and as a function of dimensionless quantities $\frac{l_{sf}}{L}$ and $\frac{R^s_{ch}}{R_b}$. (**D**) Calculated MR using spin polarizations $\gamma_L = \gamma_{Ni[3]} = -67\%$ and $\gamma_R(V_b) = \gamma_{NB[5]}(V_b)$ computed in (A) and taken at bias voltage V_b= −0.15 V for different values of τ_e and τ_{sf} parameters (see main text). The same data are also plotted on top of the 3D plot in (C).

Ni/molecule/outershell of the MWCNT interface. In particular, one observes that the last layer (i.e., layer [6], which corresponds to graphene and is represented by green lines in Fig. 3A) is almost unpolarized over the entire energy window considered here. At the Fermi level, the Ni outer layer has a spin polarization of about −67%. The NO_2 head and the C_6H_4 body of the NB molecules are here analyzed separately (layers [4, 5]) as the coupling with the Ni surface is mainly located in the NO_2 head of the molecule. Both have a similar spin polarization energy profile, although the NB body does not display a substantial magnetic moment. The decay of the spin-dependent hybridization away from the surface was also previously reported (*53*–*55*). From this analysis, the last spin-polarized layer is considered to be layer [5], i.e., the body of the NB molecule, except at Fermi level where the spin polarization is vanishing and where the last spin polarized layer is hence the last nickel layer, i.e., layer [3]. The FM electrode plays two major roles highlighted by those calculations. First, it induces a strong spin polarization incoming from the FM metal/molecule interface due to hybridization. Second, it also magnetically couples to spin states to the FM electrode, creating a new effective magnetic electrode with rapidly varying spin polarization around Fermi level including sign change. With the interfacial energy dependence of the spin polarizations discussed above and presented in Fig. 3A, the magnetoresistive signal can be numerically estimated. The formula developed by Seneor *et al.* [equation 3 in (*12*)] is used here, though slightly modified. To account for the potential difference across the two electrodes when applying bias voltages, the injection/detection polarizations have to be energy dependent

$$\mathrm{MR} = \frac{\gamma_L(V_L)\gamma_R(V_R)}{(1-\gamma_L(V_L)\gamma_R(V_R))} \frac{2}{2\cosh\left(\frac{L}{l_{sf}(V_b)}\right) + \left(\frac{R_b}{R^s_{ch}(V_b)} + \frac{R^s_{ch}(V_b)}{R_b}\right)\sinh\left(\frac{L}{l_{sf}(V_b)}\right)} \quad (1)$$

where $\gamma_{L/R}$ and $V_{L/R}$ are the spin polarization and bias voltage at the left/right contact interface ($V_b = V_R - V_L$, and here as the left contact is at the ground, V_L is set to zero, i.e., to the Fermi level in the calculation), L is the device length, R_b is the contact barrier, R^s_{ch} is the spin resistance of the channel, and l_{sf} is the spin diffusion length. The device length L and the contact resistance $R_b = \frac{R_{device}}{2}$ are parameters taken from the experimental measurements, assuming that both interfaces are equivalent in terms of resistance, while spin polarization $\gamma_{L/R}$ has been computed in Fig. 3A. Last, R^s_{ch} and l_{sf} can be estimated using a transport model presented in Materials and Methods and the corresponding calculations in fig. S9. The MR as expressed by Eq. 1 is composed of a product of two terms. On the one hand, the first term depends on the interface polarizations, and its value can evolve from [−0.5:+∞]. On the other hand, the second term depends on interface barrier resistance and device's properties, and its value belongs to the range [0:1]. In case of really long spin lifetime, l_{sf} becomes very large compared to L such that in Eq. 1, the hyperbolic cosine and sine functions tend to 1 and 0, respectively, which yields the second term to be maximal, i.e., 1, and offers an optimal transport regime for the MR, which reduces to the first term only

$$\mathrm{MR}^{\text{ideal channel}} = \frac{\gamma_L(V_L)\gamma_R(V_R)}{(1-\gamma_L(V_L)\gamma_R(V_R))} \quad (2)$$

It is clear from this formula that the MR can become negative only if γ_L and γ_R have opposite signs and are at maximum −50% when left and right spin polarizations reach exactly −100% and +100%, respectively. Concerning the experimentally reported negative sign of the MR, it can thus be only well explained by a change of sign in spin polarization such as the one obtained in Fig. 3A. Because of the applied bias voltage, the sign of injected spin polarization might be opposite to the interfacial spin polarization for the detection, thus leading to negative MR. It is, for instance, the case in the [−0.3; 0.0] V bias window and, to some extent, in the [+0.1;+0.3] V bias window, as visible in Fig. 3A. The fact that the experimental MR signal reaches −40% and so indicates, first, that the system is in a regime where the distance between two spin flip events is very long compared to the device length and, second, that both left and right polarizations are close to 100% but with opposite signs. Actually, in case of perfect spin polarizations ($\gamma_L = -100\%$ and $\gamma_R = +100\%$), the first term of Eq. 1 equals −1/2, and the MR formula reduces to

$$MR^{\text{ideal spin polarizations}} = -\frac{1}{2}\frac{2}{2\cosh\left(\frac{L}{l_{sf}}\right) + \left(\frac{R_b}{R^s_{ch}} + \frac{R^s_{ch}}{R_b}\right)\sinh\left(\frac{L}{l_{sf}}\right)} \quad (3)$$

for which R^s_{ch} and l_{sf} can be taken as fully free parameters to produce a dimensionless three-dimensional (3D) color plot (see Fig. 3C), which can be useful to analyze parameter regions where MR can be highly negative. Consequently, even in case of perfect polarizations, Eq. 3 suggests that to obtain MR values such as [−50; −40]% (yellow, red color), l_{sf} needs to be at least 10 times larger than L ideally when $R^s_{ch} \approx R_b$ [as discussed in (*28*)] but should be actually 10^4 times larger than L when $\frac{R^s_{ch}}{R_b} \approx 10^{-4}$ or 10^4. As reported in Eq. 4 presented in Materials and Methods, R^s_{ch} and l_{sf} are actually not free parameters but interdependent variables and related to parameters τ_e and τ_{sf}, the charge and spin mean scattering times, respectively. Moreover, in the present situation, the contact resistance R_b is very high because of the presence of the NB molecular layer at the interface (*34*), as shown in the left-hand side of Fig. 3C.

As mentioned above, it is possible using Eq. 1 to numerically evaluate the MR signal using the DFT calculated interface polarizations together with a transport model based on tight-binding simulations and on two freely adjustable parameters τ_e and τ_{sf}. We performed such numerical estimation of the MR [see Fig. 4 and the dotted lines on top of the 3D colored plot in Fig. 3 (C and D) corresponding to a specific bias voltage of −0.15 V] using four values of charge scattering time, i.e., τ_e=80 fs, 800 fs, 8 ps, and 80 ps, and, for each of them, four values of spin scattering time, i.e., $\tau_{sf} = 10$, 10^2, 10^3, and 10^4 times the value of τ_e. The sets of two free parameters that give the largest negative MR are $\tau_e = 80$ ps and $\tau_{sf} = 10^4\,\tau_e = 800$ ns. The corresponding simulated MR curve is presented in Fig. 4 (blue line) together with the experimental data of sample A with Ni electrodes. As mentioned earlier, the corresponding transport properties of the model are displayed in fig. S9, including the bias-dependent mean free path and spin diffusion length (l_e and l_{sf}), which are found in the range [26 to 42] μm and [4 to 6] mm, respectively. The estimated spin lifetime τ_{sf} is thus one order of magnitude higher compared with the recent reported values measured for encapsulated graphene (*56*). Such extremely long spin diffusion lengths could be interpreted as follows: The spin-polarized electrons are transferred from the FM electrode to the inner shells of the MWCNT passing through

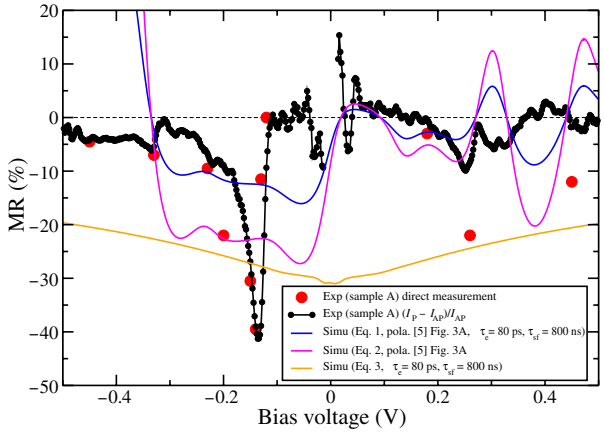

Fig. 4. Experimental and simulated MR bias voltage dependence. Experimental data correspond to the ones presented in Fig. 2D. Simulated MR curves at different bias voltage using Eq. 1 with polarizations obtained in Fig. 3A, i.e., $\gamma_L = \gamma_{Ni[3]}(E_F) = -67\%$ and $\gamma_R(V_b) = \gamma_{NB[5]}(V_b)$ and parameters $\tau_e = 80$ ps and $\tau_{sf} = 800$ ns for the channel (blue line); Eq. 2 with polarizations obtained in Fig. 3A, i.e., $\gamma_L = \gamma_{Ni[3]}(E_F) = -67\%$ and $\gamma_R(V_b) = \gamma_{NB[5]}(V_b)$ and ideal channel (purple line); and Eq. 3 with ideal polarizations and parameters $\tau_e = 80$ ps and $\tau_{sf} = 800$ ns for the channel (orange line).

an efficient spin filtering FM electrode/NB-functionalized outershell interface. Once in the inner shells, the charges and spins are protected and conveniently transported toward the second magnetic electrode, where the spin information is electrically converted because of a magnetoresistive effect. The fact that the spin polarization is rendered bias voltage dependent with such a rapidly varying sign around the Fermi level due to the NB molecule allows us to interpret the change of sign of the measured MR with respect to the applied bias voltage. The simulations performed predict a change of sign for bias voltage windows ~[−300; 0] mV and ~[+100; +300] mV in line with the measurements. One shall also mention that we voluntarily limit ourselves in the values of the free adjustable parameters τ_e and τ_{sf} (at maximum 80 ps and 800 ns, respectively), which limits the numerical MR to −15% when using DFT-computed polarizations (see blue line in Fig. 4) and up to −30% if one uses ideal polarizations of −100% and 100% as in Eq. 3 (see orange line in Fig. 4). To complete this analysis of the model, we also plot the numerical MR estimated using DFT polarizations but with ideal channel as in Eq. 2 (see purple line in Fig. 4). Obviously, with ideal polarizations and ideal channel, a negative MR of −50% would be obtained for all bias voltages. The analysis provided in Fig. 4 demonstrates that numerical MR strongly depends on interface spin polarization, which, in turn, strongly depends on the precise molecular interaction with the FM surface. Figure S10 illustrates this dependence of the MR on the Ni/NB molecule interaction through an analysis of the spin polarization energy profile and the corresponding MR for each NB molecule individually. For instance, taking only molecules in sublattice A yields a numerical MR almost solely positive (see the blue line with square symbols in fig. S10D). Although the atomic positions of the atoms were relaxed, the starting position was randomly chosen, and one cannot exclude other Ni/NB molecule interface scenarios not investigated here, which could enhance the injection/detection spin polarization. Local A and B sublattice unbalance could also occur a priori in rare cases, yielding possibly to local polarization of the outershell layer as depicted in fig. S11. For the sake of completeness, the case of a direct Ni/graphene

interface is also investigated in fig. S13. Again, this scenario should be nondominant, as the molecular covering is sufficiently high such that Ni atoms are normally not in direct contact with the outer-shell of the MWCNT. As in fig. S11, the graphene layer becomes the last polarized layer due to a small magnetic moment induced in graphene by proximity effect. Nevertheless, no negative MR is reported in the bias windows of interest. The transport properties and the MR equation are obtained from models that have their own limitations concerning absolute values, which prompt us to use not too optimistic values τ_e and τ_{sf}, although the very generic forms of the models still allow us to demonstrate that spin lifetime should, in any case, be extremely long to reach an MR effect of −40%.

Last, concerning the temperature dependence of the MR effect, it vanishes rapidly around 30 K as observed in sample A (see fig. S12). It is a quite rapid extinction of the MR even if not completely different compared to more standard MWCNT-based spin-valves (*20*, *29*) or with organic magnetic junctions (*36*, *57*) for which MR effects can subsist at slightly higher temperatures. Because of the high curie temperature of the Co and Ni electrodes, the loss of magnetization is unexpected. Concerning the hybridization and the induced magnetic coupling of the hybridized spin states with the FM surface, it is also expected to survive up to room temperature (*58*). A temperature-activated spin scattering mechanism during the transport along the inner shells of the MWCNT could be invoked. The physical origin of the strong influence of the temperature in those systems remains an open question. Only the positive part assigned to the TAMR signal remains at 30 K, thus strongly reinforcing the given interpretation of two distinct MR components (TAMR and spin-valve) originating from different phenomena.

CONCLUSION

Intense magnetoresistive signals of −40% close to the theoretical limit of −50% have been reported in MWCNTs functionalized with NB molecules. Within the framework of a spin transport model optimized for confined geometries, those values of the spin signal are interpreted as spin transport occurring over millimetric distances. The spin transport model has also been extended by inserting an energy dependence of the spin polarization of the electrodes, allowing more accurate understanding of the peculiar bias voltage dependence reported in these carbon-based complex nanosystems. The reported amplitude of the magnetoresistive signal and its bias dependence are finally ascribed to the spin-dependent hybridization of the molecular states producing extremely high spin polarizations.

MATERIALS AND METHODS

Chemical functionalization

The chemical vapor–deposited MWCNTs with large diameters (>60 nm) are purchased from MER Corporation. Their length is limited to few micrometers. The molecular layer at the surface of the MWCNTs is grown by chemical reaction with NBD molecules. The radical moieties spontaneously reduce at the surface of MWCNTs forming C—C covalent bonds with their outermost shell. This reaction is performed in solution. The molecular layer covers the outermost shell. The protocol used here is a 24-hour reaction with a high NBD concentration ($[C] = 10^{-1}$ M) and photoactivation (100 W of visible light during the first hour). As described previously in (*34*), this functionalization protocol induces a dense molecular layer.

Device nanofabrication

Once functionalized, the MWCNTs are dispersed over a Si/SiO_2 (500 nm) substrate and individually contacted by e-beam lithography (10-kV acceleration) and evaporation (deposition rate = 0.05 nm s^{-1}, $P \approx 10^{-7}$ mbar). For the purpose of spin transport applications, the electrodes are made of 130 nm (180 nm) of Ni (Co) for sample A (B), covered by a 20-nm-thick Au protecting layer to prevent oxidation. The selective switching of their magnetizations is obtained by tuning the shape anisotropy with different electrode widths (500 and 200 nm). The electrode separation is 900 nm for sample A and 800 nm for sample B. The diameters of the MWCNTs are 150 nm for sample A and 120 nm for sample B.

Measurement setup

The measurement setup is a standard DC current-voltage characterization in which the measured current is amplified by a low-noise *I-V* converter. It is combined with a conductance-voltage characterization by heterodyne detection of a small AC component (1 to 5 mV, $f \approx 100$ Hz) superimposed to the DC signal. The results presented were obtained in two different cryostats: an Oxford Instruments SM 4000-8 cryostat ($T = 1.5$ K, $P \approx 10^{-5}$ mbar) for sample A and a Montana C2 cryostat ($T = 3.1$ K, $P \approx 10^{-4}$ mbar) for sample B. In both experiments, the magnetic field is aligned along the easy magnetization axis of the FM electrodes. This configuration, in concert with shape anisotropy, allows the device to work in a spin-valve configuration.

Test measurements

A test device was realized on a Si/SiO_2 (280 nm) substrate with a large-diameter MWCNT without any molecular functionalization and with Ni electrodes following the same deposition conditions than for sample A. The channel length was 550 nm. It has been electrically tested at low temperatures (5 K), and it did not reveal any MR effect for bias voltages ranging between ±200 mV. The zero bias device's resistance was 35 kilohms. Magnetotransport measurements have been widely explored and discussed in this peculiar regime in previous studies (*29*, *31*).

Simulation methods

The electronic structure properties were carried out using ab initio DFT simulations with the SIESTA code (*59*). Spin-polarized calculations were performed using Generalized Gradient Approximation (GGA)–Perdew Burke Ernzerhof (PBE) functional with at least 15-Å vacuum distance in the vertical direction, a mesh cutoff of 300 to 500 rydberg for defining the real-space grid, and an electronic temperature of 300 K for Fermi-Dirac occupation. Atomic positions are relaxed (except for the first Ni atomic layer of the slab, which was kept fixed at bulk positions) using a conjugated gradient approach with maximum force on atoms of 0.01 eV/Å. For hexagonal 5 × 5 graphene supercells in Fig. 1 (lattice parameter and angle: 12.295 Å and 60°, respectively; 100 C atoms), a grid of *k*-point 48 × 48 × 1 was used. For square graphene supercells with Ni (100) slab in Fig. 3 and figs. S2, S10, and S11 (lattice parameter and angle: 17.843 Å and 90°, respectively; 120 C atoms), a grid of *k*-point 2 × 2 × 1 was used. The Ni slab is composed of three layers containing 50 Ni atoms each.

The transport model was based on the following set of equations and used to calculate the parameters R^{s}_{ch} and l_{sf} inserted in Eq. 1

$$l_{sf}(V_b) = \frac{1}{e\ |\ V_b\ |}\int_{eV_L}^{eV_R} l_{sf}(E)\,dE \quad (4)$$

$$R^{s}_{ch}(V_b) = \frac{1}{e\ |\ V_b\ |}\int_{eV_L}^{eV_R} R^{s}_{ch}(E)\,dE \quad (5)$$

$$R^{s}_{ch}(E) = \rho(E)\, l_{sf}(E) \quad (6)$$

$$\rho(E) = \frac{1}{\sigma(E)} \quad (7)$$

$$\sigma(E) = \frac{1}{2} e^2\, DOS(E)\, D(E) \quad (8)$$

$$l_{sf}(E) = \sqrt{D(E)\,\tau_{sf}} \quad (9)$$

$$D(E) = 2v(E)\, l_e(E) \quad (10)$$

$$l_e(E) = v(E)\,\tau_e \quad (11)$$

where τ_e and τ_{sf} are the free adjustable parameters, constant in energy, corresponding to the charge and spin lifetime; l_e and l_{sf} are the associated mean free paths; D and v are the charge carrier diffusion coefficient and velocity, respectively; DOS is the nanotube density of states per unit of length; and σ and ρ are the nanotube conductivity and resistivity, respectively. The energy-dependent density of states and charge carrier velocity of a pristine zigzag triple-wall CNT (TWCNT) of ~80 nm diameter, more precisely a (1045,0)@(1054,0)@(1063,0) TWCNT, were previously computed using tight-binding calculations in (*60*). All these quantities, as obtained with parameters $\tau_e = 80 \times 10^{-12}$ s and $\tau_{sf} = 10^4 \times \tau_e = 800 \times 10^{-9}$ s, can be found in fig. S9.

SUPPLEMENTARY MATERIALS

Supplementary material for this article is available at http://advances.sciencemag.org/cgi/content/full/6/31/eaba5494/DC1

REFERENCES AND NOTES

1. B. Behin-Aein, D. Datta, S. Salahuddin, S. Datta, Proposal for an all-spin logic device with built-in memory. *Nat. Nanotechnol.* **5**, 266–270 (2010).
2. M. G. Mankalale, S. S. Sapatnekar, Optimized standard cells for all-spin logic. *ACM J. Emerg. Technol. Comput. Syst.* **13**, 1–22 (2016).
3. A. A. Khajetoorians, J. Wiebe, B. Chilian, R. Wiesendanger, Realizing all-spin-based logic operations atom by atom. *Science* **332**, 1062–1064 (2011).
4. L. Su, W. Zhao, Y. Zhang, D. Querlioz, Y. Zhang, J. O. Klein, P. Dollfus, A. Bournel, Proposal for a graphene-based all-spin logic gate. *Appl. Phys. Lett.* **106**, 072407 (2015).
5. Y. Tserkovnyak, A. Brataas, G. E. W. Bauer, Spin pumping and magnetization dynamics in metallic multilayers. *Phys. Rev. B* **66**, 224403 (2002).
6. K. Uchida, S. Takahashi, K. Harii, J. Ieda, W. Koshibae, K. Ando, S. Maekawa, E. Saitoh, Observation of the spin Seebeck effect. *Nature* **455**, 778–781 (2008).
7. T. Jungwirth, J. Wunderlich, K. Olejník, Spin Hall effect devices. *Nat. Mater.* **11**, 382–390 (2012).
8. T. Taniyama, E. Wada, M. Itoh, M. Yamaguchi, Electrical and optical spin injection in ferromagnet/semiconductor heterostructures. *NPG Asia Mater.* **3**, 65–73 (2011).
9. L. J. Cornelissen, J. Liu, R. A. Duine, J. Ben Youssef, B. J. van Wees, Long-distance transport of magnon spin information in a magnetic insulator at room temperature. *Nat. Phys.* **11**, 1022–1026 (2015).
10. F. J. Jedema, M. V. Costache, H. B. Heersche, J. J. A. Baselmans, B. J. van Wees, Electrical detection of spin accumulation and spin precession at room temperature in metallic spin valves. *Appl. Phys. Lett.* **81**, 5162–5164 (2002).
11. M. Johnson, R. H. Silsbee, Spin-injection experiment. *Phys. Rev. B* **37**, 5326–5335 (1988).
12. P. Seneor, B. Dlubak, M.-B. Martin, A. Anane, H. Jaffres, A. Fert, Spintronics with graphene. *MRS Bull.* **37**, 1245–1254 (2012).
13. J. C. Leutenantsmeyer, J. Ingla-Aynés, J. Fabian, B. J. Van Wees, Observation of spin-valley-coupling-induced large spin-lifetime anisotropy in bilayer graphene. *Phys. Rev. Lett.* **121**, 127702 (2018).
14. J. Xu, T. Zhu, Y. K. Luo, Y.-M. Lu, R. K. Kawakami, Strong and tunable spin-lifetime anisotropy in dual-gated bilayer graphene. *Phys. Rev. Lett.* **121**, 127703 (2018).
15. J. J. van den Berg, R. Yakimova, B. J. van Wees, Spin transport in epitaxial graphene on the C-terminated (000 $^{-}$ 1)-face of silicon carbide. *Appl. Phys. Lett.* **109**, 012402 (2016).
16. J. Xu, S. Singh, J. Katoch, G. Wu, T. Zhu, I. Žutić, R. K. Kawakami, Spin inversion in graphene spin valves by gate-tunable magnetic proximity effect at one-dimensional contacts. *Nat. Commun.* **9**, 2869 (2018).
17. W. Han, K. Pi, K. M. McCreary, Y. Li, J. J. I. Wong, A. G. Swartz, R. K. Kawakami, Tunneling spin injection into single layer graphene. *Phys. Rev. Lett.* **105**, 167202 (2010).
18. M. V. Kamalakar, C. Groenveld, A. Dankert, S. P. Dash, Long distance spin communication in chemical vapour deposited graphene. *Nat. Commun.* **6**, 6766 (2015).
19. M. Gurram, S. Omar, B. J. van Wees, Electrical spin injection, transport, and detection in graphene-hexagonal boron nitride van der Waals heterostructures: Progress and perspectives. *2D Mater.* **5**, 032004 (2018).
20. L. E. Hueso, J. M. Pruneda, V. Ferrari, G. Burnell, J. P. Valdés-Herrera, B. D. Simons, P. B. Littlewood, E. Artacho, A. Fert, N. D. Mathur, Transformation of spin information into large electrical signals using carbon nanotubes. *Nature* **445**, 410–413 (2007).
21. B. Dlubak, M.-B. Martin, C. Deranlot, B. Servet, S. Xavier, R. Mattana, M. Sprinkle, C. Berger, W. A. De Heer, F. Petroff, A. Anane, P. Seneor, A. Fert, Highly efficient spin transport in epitaxial graphene on SiC. *Nat. Phys.* **8**, 557–561 (2012).
22. W. Han, R. K. Kawakami, M. Gmitra, J. Fabian, Graphene spintronics. *Nat. Nanotechnol.* **9**, 794–807 (2014).
23. A. R. Rocha, V. M. García-Suárez, S. W. Bailey, C. J. Lambert, J. Ferrer, S. Sanvito, Towards molecular spintronics. *Nat. Mater.* **4**, 335–339 (2005).
24. B. Dlubak, P. Seneor, A. Anane, C. Barraud, C. Deranlot, D. Deneuve, B. Servet, R. Mattana, F. Petroff, A. Fert, Are Al_2O_3 and MgO tunnel barriers suitable for spin injection in graphene? *Appl. Phys. Lett.* **97**, 092502 (2010).
25. M. V. Kamalakar, A. Dankert, J. Bergsten, T. Ive, S. P. Dash, Enhanced tunnel spin injection into graphene using chemical vapor deposited hexagonal boron nitride. *Sci. Rep.* **4**, 6146 (2015).
26. Q. Wu, L. Shen, Z. Bai, M. Zeng, M. Yang, Z. Huang, Y. P. Feng, Efficient spin injection into graphene through a tunnel barrier: Overcoming the spin-conductance mismatch. *Phys. Rev. Appl.* **2**, 044008 (2014).
27. E. I. Rashba, Theory of electrical spin injection: Tunnel contacts as a solution of the conductivity mismatch problem. *Phys. Rev. B* **62**, R16267–R16270 (2000).
28. H. Jaffrès, J.-M. George, A. Fert, Spin transport in multiterminal devices: Large spin signals in devices with confined geometry. *Phys. Rev. B* **82**, 140408 (2010).
29. C. Morgan, M. Misiorny, D. Metten, S. Heedt, T. Schäpers, C. M. Schneider, C. Meyer, Impact of tunnel-barrier strength on magnetoresistance in carbon nanotubes. *Phys. Rev. Appl.* **5**, 054010 (2016).
30. K. Tsukagoshi, B. W. Alphenaar, H. Ago, Coherent transport of electron spin in a ferromagnetically contacted carbon nanotube. *Nature* **401**, 572–574 (1999).
31. B. Zhao, I. Mönch, H. Vinzelberg, T. Mühl, C. M. Schneider, Spin-coherent transport in ferromagnetically contacted carbon nanotubes. *Appl. Phys. Lett.* **80**, 3144–3146 (2002).
32. J. Samm, J. Gramich, A. Baumgartner, M. Weiss, C. Schönenberger, Optimized fabrication and characterization of carbon nanotube spin valves. *J. Appl. Phys.* **115**, 174309 (2014).
33. V. M. Karpan, G. Giovannetti, P. A. Khomyakov, M. Talanana, A. A. Starikov, M. Zwierzycki, J. van den Brink, G. Brocks, P. J. Kelly, Graphite and graphene as perfect spin filters. *Phys. Rev. Lett.* **99**, 176602 (2007).
34. R. Bonnet, C. Barraud, P. Martin, M. L. Della Rocca, P. Lafarge, Inducing injection barrier by covalent functionalization of multiwall carbon nanotubes acting as Moiré crystals. *Appl. Phys. Lett.* **109**, 143110 (2016).
35. N. Atodiresei, J. Brede, P. Lazić, V. Caciuc, G. Hoffmann, R. Wiesendanger, S. Blügel, Design of the local spin polarization at the organic-ferromagnetic interface. *Phys. Rev. Lett.* **105**, 066601 (2010).
36. C. Barraud, P. Seneor, R. Mattana, S. Fusil, K. Bouzehouane, C. Deranlot, P. Graziosi, L. Hueso, I. Bergenti, V. Dediu, F. Petroff, A. Fert, Unravelling the role of the interface for spin injection into organic semiconductors. *Nat. Phys.* **6**, 615–620 (2010).
37. D. Bouilly, J. Cabana, F. Meunier, M. Desjardins-Carrière, F. Lapointe, P. Gagnon, F. L. Larouche, E. Adam, M. Paillet, R. Martel, Wall-selective probing of double-walled carbon nanotubes using covalent functionalization. *ACS Nano* **5**, 4927–4934 (2011).
38. J. Pinson, F. Podvorica, Attachment of organic layers to conductive or semiconductive surfaces by reduction of diazonium salts. *Chem. Soc. Rev.* **34**, 429–439 (2005).
39. E. J. G. Santos, A. Ayuela, D. Sánchez-Portal, Universal magnetic properties of sp^3-type defects in covalently functionalized graphene. *New J. Phys.* **14**, 043022 (2012).

40. H. González-Herrero, J. M. Gómez-Rodríguez, P. Mallet, M. Moaied, J. J. Palacios, C. Salgado, M. M. Ugeda, J.-Y. Veuillen, F. Yndurain, I. Brihuega, Atomic-scale control of graphene magnetism by using hydrogen atoms. *Science* **352**, 437–441 (2016).
41. D. Soriano, N. Leconte, P. Ordejón, J.-C. Charlier, J.-J. Palacios, S. Roche, Magnetoresistance and magnetic ordering fingerprints in hydrogenated graphene. *Phys. Rev. Lett.* **107**, 016602 (2011).
42. A. V. Rudnev, V. Kaliginedi, A. Droghetti, H. Ozawa, A. Kuzume, M.-A. Haga, P. Broekmann, I. Rungger, Stable anchoring chemistry for room temperature charge transport through graphite-molecule contacts. *Sci. Adv.* **3**, e1602297 (2017).
43. M. Cinchetti, V. A. Dediu, L. E. Hueso, Activating the molecular spinterface. *Nat. Mater.* **16**, 507–515 (2017).
44. C. Schönenberger, A. Bachtold, C. Strunk, J. P. Salvetat, L. Forró, Interference and interaction in multi-wall carbon nanotubes. *Appl. Phys. A Mater. Sci. Process.* **69**, 283–295 (1999).
45. M. Grünewald, M. Wahler, F. Schumann, M. Michelfeit, C. Gould, R. Schmidt, F. Würthner, G. Schmidt, L. W. Molenkamp, Tunneling anisotropic magnetoresistance in organic spin valves. *Phys. Rev. B* **84**, 125208 (2011).
46. C. Gould, C. Rüster, T. Jungwirth, E. Girgis, G. M. Schott, R. Giraud, K. Brunner, G. Schmidt, L. W. Molenkamp, Tunneling anisotropic magnetoresistance: A spin-valve-like tunnel magnetoresistance using a single magnetic layer. *Phys. Rev. Lett.* **93**, 117203 (2004).
47. K. V. Raman, A. M. Kamerbeek, A. Mukherjee, N. Atodiresei, T. K. Sen, P. Lazić, V. Caciuc, R. Michel, D. Stalke, S. K. Mandal, S. Blügel, M. Münzenberg, J. S. Moodera, Interface-engineered templates for molecular spin memory devices. *Nature* **493**, 509–513 (2013).
48. C. Barraud, K. Bouzehouane, C. Deranlot, S. Fusil, H. Jabbar, J. Arabski, R. Rakshit, D.-J. J. Kim, C. Kieber, S. Boukari, M. Bowen, E. Beaurepaire, P. Seneor, R. Mattana, F. Petroff, Unidirectional spin-dependent molecule-ferromagnet hybridized states anisotropy in cobalt phthalocyanine based magnetic tunnel junctions. *Phys. Rev. Lett.* **114**, 206603 (2015).
49. M. Jullière, Tunneling between ferromagnetic films. *Phys. Lett. A* **54**, 225–226 (1975).
50. J. S. Moodera, G. Mathon, Spin polarized tunneling in ferromagnetic junctions. *J. Magn. Magn. Mater.* **200**, 248–273 (1999).
51. M. Galbiati, S. Tatay, C. Barraud, A. V. Dediu, F. Petroff, R. Mattana, P. Seneor, Spinterface: Crafting spintronics at the molecular scale. *MRS Bull.* **39**, 602–607 (2014).
52. S. Schmaus, A. Bagrets, Y. Nahas, T. K. Yamada, A. Bork, M. Bowen, E. Beaurepaire, F. Evers, W. Wulfhekel, Giant magnetoresistance through a single molecule. *Nat. Nanotechnol.* **6**, 185–189 (2011).
53. A. Droghetti, P. Thielen, I. Rungger, N. Haag, N. Großmann, J. Stöckl, B. Stadtmüller, M. Aeschlimann, S. Sanvito, M. Cinchetti, Dynamic spin filtering at the Co/Alq3 interface mediated by weakly coupled second layer molecules. *Nat. Commun.* **7**, 12668 (2016).
54. T. Moorsom, M. Wheeler, T. Mohd Khan, F. Al Ma'Mari, C. Kinane, S. Langridge, D. Ciudad, A. Bedoya-Pinto, L. Hueso, G. Teobaldi, V. K. Lazarov, D. Gilks, G. Burnell, B. J. Hickey, O. Cespedes, Spin-polarized electron transfer in ferromagnet/C_{60} interfaces. *Phys. Rev. B* **90**, 125311 (2014).
55. Q. Arnoux, C. Blouzon, D. Li, Y. J. Dappe, A. Smogunov, P. Bonville, L. Tortech, J.-B. Moussy, Controlling the magnetic exchange coupling in hybrid heterojunctions via spacer layers of π -conjugated molecules. *Phys. Rev. B* **99**, 144405 (2019).
56. M. Drögeler, C. Franzen, F. Volmer, T. Pohlmann, L. Banszerus, M. Wolter, K. Watanabe, T. Taniguchi, C. Stampfer, B. Beschoten, Spin lifetimes exceeding 12 ns in graphene nonlocal spin valve devices. *Nano Lett.* **16**, 3533–3539 (2016).
57. F. J. Wang, Z. H. Xiong, D. Wu, J. Shi, Z. V. Vardeny, Organic spintronics: The case of Fe/Alq3/Co spin-valve devices. *Synth. Met.* **155**, 172–175 (2005).
58. M. Gruber, F. Ibrahim, S. Boukari, L. Joly, V. Da Costa, M. Studniarek, M. Peter, H. Isshiki, H. Jabbar, V. Davesne, J. Arabski, E. Otero, F. Choueikani, K. Chen, P. Ohresser, W. Wulfhekel, F. Scheurer, E. Beaurepaire, M. Alouani, W. Weber, M. Bowen, Spin-dependent hybridization between molecule and metal at room temperature through interlayer exchange coupling. *Nano Lett.* **15**, 7921–7926 (2015).
59. J. M. Soler, E. Artacho, J. D. Gale, A. García, J. Junquera, P. Ordejón, D. Sánchez-Portal, The SIESTA method for *ab initio* order- *N* materials simulation. *J. Phys. Condens. Matter* **14**, 2745–2779 (2002).
60. R. Bonnet, A. Lherbier, C. Barraud, M. L. D. Rocca, P. Lafarge, J.-C. Charlier, Charge transport through one-dimensional Moiré crystals. *Sci. Rep.* **6**, 19701 (2016).

Acknowledgments: We acknowledge C. Manquest and P. Filloux for technical support within the clean room of the Laboratoire Matériaux et Phénomènes Quantiques (UMR 7162) at the University of Paris. We acknowledge P. Seneor, R. Mattana, B. Dlubak, and F. Petroff for their help concerning the transport measurements of sample A and the scientific discussion. We also acknowledge G. Wang for his help during the TEM measurements and J. Rastikian for her help during the test measurements. **Funding:** C.B. acknowledges financial support from the Ville de Paris "Emergence" program ("2DSPIN" project) and from the Région Ile-de-France in the framework of DIM Nano-K through the research project "Spin transport at the Molecular Scale" project. A.L. and J.-C.C. acknowledge financial support from the Fédération Wallonie-Bruxelles through the ARC on 3D nanoarchitecturing of 2D crystals (no. 16/21-077), the European Union's Horizon 2020 Research Project and Innovation Program (Graphene Flagship Core1 no. 696656 and Core2 no. 785219), the Francqui-Stichting Foundation, and the Belgium FNRS through research project nos. T.1077.15 and R.50.07.18.F. Computational resources have been provided by the supercomputing facilities (CISM) of the Université catholique de Louvain (UCLouvain) and the Consortium des Équipements de Calcul Intensif en Fédération Wallonie Bruxelles (CÉCI) funded by the Fond de la Recherche Scientifique de Belgique (F.R.S.-FNRS) under convention no. 2.5020.11. **Author contributions:** All authors have contributed to the general scientific discussion and to the writing of the manuscript. R.B., P.M., S.S., P.L., M.L.D.R., and C.B. conducted the experimental part. C.B., P.M., and R.B. developed the molecular functionalization process. C.B., S.S., and R.B. developed the micro- and nanofabrication process. A.L. and J.-C.C. conducted all the theoretical calculations and analysis. **Competing interests:** The authors declare that they have no competing interests. **Data and materials availability:** All data needed to evaluate the conclusions in the paper are present in the paper and/or the Supplementary Materials. Additional data related to this paper may be requested from the authors.

Submitted 12 December 2019
Accepted 17 June 2020
Published 31 July 2020
10.1126/sciadv.aba5494

Citation: R. Bonnet, P. Martin, S. Suffit, P. Lafarge, A. Lherbier, J.-C. Charlier, M. L. Della Rocca, C. Barraud, Giant spin signals in chemically functionalized multiwall carbon nanotubes. *Sci. Adv.* **6**, eaba5494 (2020).

Science Advances

Giant spin signals in chemically functionalized multiwall carbon nanotubes

Roméo Bonnet, Pascal Martin, Stéphan Suffit, Philippe Lafarge, Aurélien Lherbier, Jean-Christophe Charlier, Maria Luisa Della Rocca and Clément Barraud

Sci Adv **6** (31), eaba5494.
DOI: 10.1126/sciadv.aba5494